Advection-based multiframe iterative correction on PIV fields for improved pressure estimation

Chen Junwei*

Department of Aerospace Engineering, Universidad Carlos III de Madrid, Avda. Universidad 30, 28911, Leganes, Spain
*Corresponding author: junwei.chen@uc3m.es

Keywords: PIV processing, pressure, post processing, data assimilation.

ABSTRACT

A novel method to improve the accuracy of pressure field estimation for advection-dominated flows from time-resolved Particle Image Velocimetry (PIV) data is proposed. Leveraging an advection model we can propagate in time velocity fields from each snapshot. The multiple time-series obtained from time propagation are used to smooth the nonphysical features in the original time-series. This correction is done iteratively. The technique reduces spatial noise by leveraging temporal information while simultaneously correcting temporal jitters using spatial data. Two validation methods are proposed to evaluate the method without knowing the true value of the pressure field. In this paper we provide a proof of concept using a 3D synthetic dataset based on channel flow and a 2D PIV data set on the wake of a wing foil. Various noise models are tested by superimposing them onto the synthetic dataset, including Gaussian white noise and errors with spatial coherence. The results demonstrate that the proposed method outperforms conventional filters in improving the velocity and pressure fields from noisy velocity data, and in suppressing time jittering of the estimated pressure fields.

1. Introduction

Owing to the development of PIV (Particle Image Velocimetry) techniques in recent decades, non-intrusive pressure field estimation became feasible. Time-resolved velocity fields can be plugged in the Navier-Stokes equations to determine the pressure gradient field, or alternatively the Poisson equation of pressure can be solved. However, uncertainty is inevitably existed in the PIV data (Sciacchitano, 2019) and amplified during the finite differentiation when calculating pressure (Azijli et al., 2016; Zhang et al., 2022). High-quality PIV measurement and processing is essential to achieve accurate pressure field. This is however not always possible.

Post-processing of PIV data is used to remove the noise and improve the quality of the velocity field. Common approaches involve applying the filters to suppress the jittering of the data, which can be done by the convolution in space-temporal domain, such as Gaussian filter, Savitzky-Golay

(SG) filter, filters in the Fourier space (Foucaut & Stanislas, 2002), or Proper Orthogonal Decomposition (POD) (Raiola et al., 2015). These solutions are often integrated with data assimilation techniques, where governing equations are utilized to regularize the flow field. By incorporating the full Navier-Stokes equations, the optimization process for velocity and pressure field correction can be directly refined. This can be considered as a constrained optimization problem and solved with adjoint approach, as the assimilation for compressible flow by Lemke & Sesterhenn (2016), and that with super-resolution technique developed by He et al. (2024). A simpler and computationally-affordable alternative is based on solenoidal filtering to impose only divergence-free conditions on incompressible flows (de Silva et al., 2013). Other widely-used regularization methods include the vortex in cell (VIC) method specialized for 3D flow field (Christiansen, 1973; Schneiders et al., 2014; Scarano et al., 2022), based on vorticity transport for an inviscid incompressible fluid, and B-Spline or radial basis function regression from particle tracks (Gesemann, 2015; Sperotto et al., 2022).

With the developments in the infrastructure of hardware and algorithms, machine learning becomes a practical approach to assist PIV processing. Focusing on the post processing of vector fields, techniques like convolutional neural networks (CNNs), autoencoders (AE) and Physics Informed Neural Network (PINN) are used to filter noise (Gu et al., 2024), resolution enhancement (Liu et al., 2020), interpolate missing data, and correct errors (Scherl et al., 2020) in flow fields. These methods enable the extraction of essential flow features while maintaining data integrity. The integration of machine learning into PIV post-processing automates the analysis, providing more reliable and precise fluid dynamics insights.

Data assimilation methods require availability of complete data, with both temporal and spatial resolution. There might be cases where this is not possible (e.g. planar PIV), which opens up the question on whether simpler models can still be reasonably effective in certain conditions. Advection models can be a promising candidate, considering its success in supplementing the temporal derivative component for pressure calculation in snapshot PIV (de Kat & Ganapathisubramani, 2012; Van der Kindere et al., 2019). This approach could in principle also be leveraged to regularize the velocity fields.

In this study, we introduce an Advection-based Multiframe Iterative Correction (AMIC) method designed to regularize time-resolved PIV fields in advection-dominated flows. By employing an advection model for the fluctuating part, the velocity fields can be propagated forward and backward in time. This generates multiple parallel time-series of velocity fields, facilitating filtering among the parallel fields at a single vector and single snapshot scale. An iterative correction process is then applied to regularize the velocity fields, which also presents enhancements in pressure estimation accuracy.

The proposed method as well as the conventional methods for comparison will be explained in Sec. 2. After that, the testing datasets, a 3D simulation and a planar PIV test, will be described in

Sec. 3. Then the results are discussed in Sec. 4.

2. Method

2.1. Advection-based Multiframe Iterative Correction

The proposed AMIC is based on filtering the velocity field along an additional dimension indicating the 'Multiverse' of several time-series of the velocity field, thus avoids losing details due to filtering the field on spatial or temporal domain. The additional time series $\mathbf{u}_{gen}$ for filtering are generated from original PIV field $\mathbf{u}_{PIV}$ via an advection-based model is applied. The model is derived from Taylor's hypothesis of frozen turbulence, which assumes small-scale flow motions are advected by the large-scale motions. This can be described as the material derivative of small-scale motions being negligible,

$$\frac{D\mathbf{u}'}{Dt} = \frac{\partial \mathbf{u}'}{\partial t} + (\mathbf{u}_c \cdot \nabla)\mathbf{u}' \approx 0, \tag{1}$$

where the $\mathbf{u}_c$ is the local convective velocity, and the $\mathbf{u}'$ is the fluctuating velocity corresponding to small-scale motions. The convective velocity is primarily determined by the large-scale motions. In this study, the convective velocity is computed from low-pass spatial filtering of the instantaneous velocity fields, allowing it to effectively handle intermittent flows and flows transitioning between different states. Then, assuming that the timescale of large-scale motions is much larger than that of the small-scale motions, the approximate temporal derivative of the velocity field can be set as:

$$\frac{\partial \mathbf{u}}{\partial t} = -(\mathbf{u}_c \cdot \nabla)\mathbf{u}'. \tag{2}$$

This hypothesis is more effective for small-scale motions than for large-scale ones, and assumes that fluctuations are passively advected with a local convective velocity, without accounting for rotation and straining. It should be noticed that the governing equation can be replaced with other methods, such as full Navier-Stokes equation or VIC.

With the advection model in Eq. (2), the velocity fields are propagated in both directions using the 4^{th} order Runge-Kutta method, generating a sequence of fields with the same time separation as the original PIV recording. The nomenclature $\mathbf{u}_{gen-1}$, $\mathbf{u}_{gen+1}$, $\mathbf{u}_{gen-2}$, $\mathbf{u}_{gen+2}$, ... will be used to refer to the time-series in parallel obtained by propagating the original time-series $\mathbf{u}_{PIV}$ of one time backward and forward and two times backward and forward, respectively. Then, as dipicted in Fig. 1, the j^{th} frame in the time-series $\mathbf{u}_{PIV,j}$ is updated by the weighted average of original and propagated time-series at the same time instant,

$$\mathbf{u}_{PIV,j} \leftarrow (1 - 2\sum_{i}^{N} \lambda_i)\mathbf{u}_{PIV,j} + \sum_{i}^{N}(\lambda_i \mathbf{u}_{gen-i,j+i} + \lambda_i \mathbf{u}_{gen+i,j-i}), \tag{3}$$

where the weight coefficient λ has to comply with $0 < \lambda_i < 1$ and $(1 - 2\sum_{i}^{N} \lambda_i) > 0$. This update is implemented as an iterative process. It takes around $2s$ per frame to process using AMIC on a hexadeca core processor.

The AMIC method offers three significant advantages with respect to traditional spatio-temporal filtering. Firstly, it filters the velocity field along an additional dimension, retaining more details compared to traditional spatial and temporal filtering. Secondly, AMIC corrects time-related errors using spatial information and space-related errors using temporal information. This crosstalk reduces error sources that are completely inconsistent with physics, thus enhancing for instance pressure field predictions. Lastly, the simplicity of the advection model ensures minimal computational cost compared to more advanced data assimilation schemes. Additionally, it should be mentioned that the proposed method does not necessarily need 3D data, provided the main direction of advection is reasonably aligned within the measurement plan.

The AMIC method is compared with three widely used filtering techniques: the Savitzky-Golay filtering, optimal POD truncation, and denoising autoencoder. The benchmark methods are outlined in the next sections.

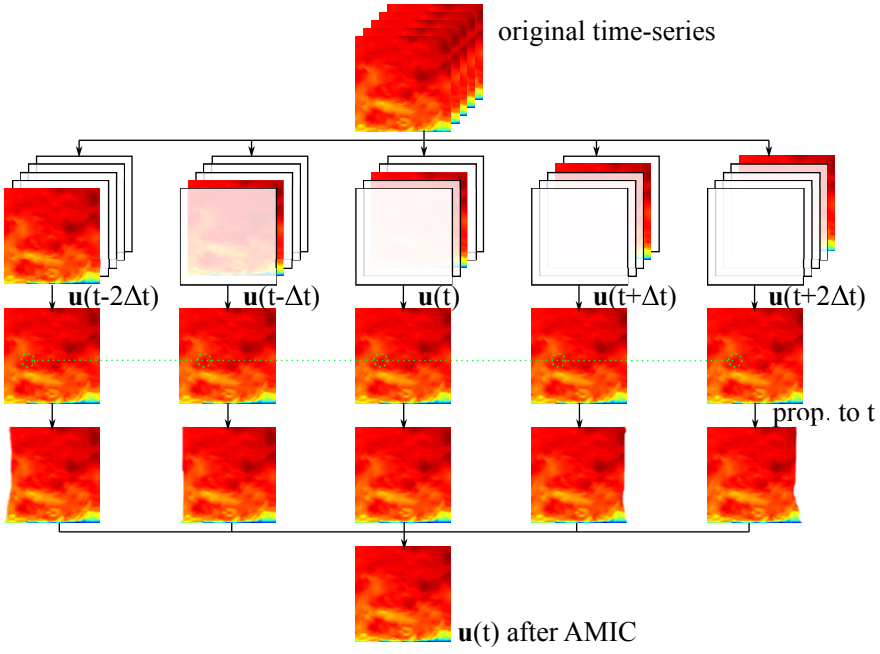

Figure 1. Conceptual sketch of the advection-based multiframe iterative correction. For simplicity a stencil of 5 snapshots in time is considered.

2.2. Savitzky-Golay filter

The Savitzky-Golay filter (Savitzky & Golay, 1964) is a widely-used technique for smoothing data by fitting low-degree local polynomials. It functions by convolving the data with a kernel derived from the linear least squares method, assuming the data points are equally spaced. In this study, 2^{nd} order Savitzky-Golay filters at $5 \times 5 \times 5 \times 5$ 4D (3D space + time) for volumetric data sets and $5 \times 5 \times 5$ 3D (2D space + time) for planar data sets, are applied to the velocity field to serve as a benchmark for the proposed AMIC method.

2.3. Proper Orthogonal Decomposition truncation

POD is a powerful mathematical tool widely used in fluid mechanics for order reduction over complex flow fields and analyze flow structures. This technique, proposed by Lumley et al. (1967), decomposes the flow into orthogonal spatial and temporal modes, with singular values indicating the variance corresponding to each mode. The POD truncation assumes that noise is high rank, thus it is distributed across the POD spectrum, while the true information's contribution is of lower rank. The true information, quickly decreasing in the POD spectrum, is overwhelmed by the noise for high-order modes. An adequate truncation aims to identify the number of modes beyond which adding more modes in the reconstruction has the effect of introducing more spurious information than physical one. Several criteria are available for the identification of the optimal cutoff; in this work we use a criterion similar to the one proposed by Raiola et al. (2015). A cut-off condition is set when the squared ratio of adjacent singular values $(\sigma_{i+1}/\sigma_i)^2 > 0.99$. To reduce sensitivity to noise due to poor convergence, we additional require that the threshold is surpasses for at least 3 consecutive mode numbers. This increases the robustness of the criterion, especially in scenarios such as 3D PIV in which the number of snapshots is limited.

2.4. Denoising autoencoders

Autoencoders, a type of artificial neural network, offer a powerful solution to effectively filter out noise. The basic architecture of autoencoders comprises an encoder, which compresses the input data into a latent space, and a decoder, which reconstructs the original input data from the encoded representation (Kramer, 1991). Autoencoders can learn to identify and remove noise while preserving important features of the velocity field, such as flow patterns and structures. During training, the autoencoder learns to encode the input velocity field into a lower-dimensional representation that captures the essential information while filtering out noise. The decoder then reconstructs the denoised velocity field from this encoded representation.

In this study, we evaluate the performance of an autoencoder for noise removal in fluid mechanics. The model size is limited here by the the available computational resources (single NVIDIA RTX

4090 with 24 GB RAM). Consequently, only one snapshot and one channel of the velocity component, regardless of its direction, is fed as input into the basic version of the autoencoder, while the cost function contains the RMS error between input and output velocity fields. This process is often referred as "blind denoising".

3. Data sets description

3.1. 3D DNS of channel flow

The performance of the proposed method is tested on a synthetic data set from JHTDB (Johns Hopkins Turbulence Databases) (Li et al., 2008). The simulation is carried out in a channel of $8\pi h \times 2h \times 3\pi h$ with h being the half-channel height, with approximately unitary bulk velocity V_b, and friction-based Reynolds number $Re_\tau \approx 1000$. The subdomain for validation is extracted with a size $h \times h \times 0.15h$ extending from the wall to the centre of the channel, and the velocity and pressure field are interpolated to a $88 \times 88 \times 12$ grid. The temporal increment of the data for validation is the same as of the database storage, given 0.0065 non-dimensional time.

Two types of noise are introduced into the volumetric velocity field of the channel flow. The first is Gaussian white noise (GWN) with a standard deviation of 25% of the root mean square (RMS) value of the fluctuating velocity. Since overlapping interrogation windows are commonly employed in PIV to achieve finer vector spacing, noise may also exhibit some spatial correlation. The second type of noise aims to model this effect. It is generated from the convolution of Gaussian white noise (CGWN) with a $\sigma = 1$ Gaussian kernel in 3D space onto the first type of noise. The standard deviation of CGWN is amplified by an empirical scale factor of 6 to align the standard deviation of the two noise types. An example of instantaneous noise distribution, alongside with the corresponding perturbed instantaneous snapshot of the wall-normal velocity component, are depicted in Fig. 2. Each subfigure of Fig. 2 presents a 2D slice of the XY-plane in the 3D field, as well as part of the ZX-plane and YZ-plane on the volume's face. It's worth noting that the wall is situated on the ZX-plane at $y = 0$.

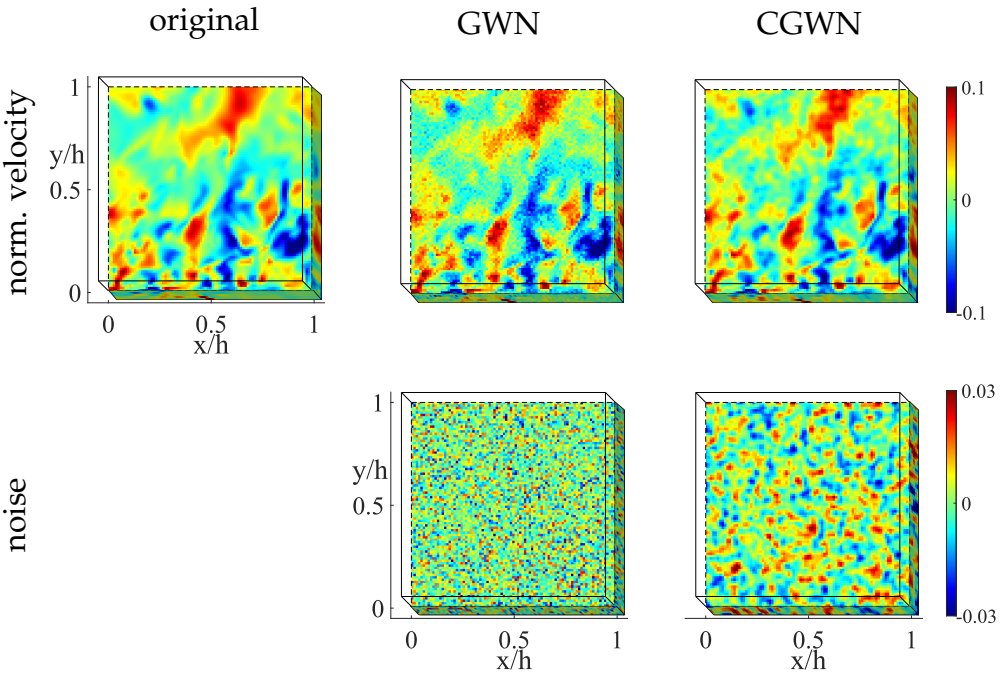

Figure 2. The wall-normal component of the velocity field (upper row) and noise added (bottom row), this figure shows the original DNS field (the left column), two types of noise, GWN (the middle column) and CGWN (the right column).

The testing dataset is composed of 100 frames of the velocity and pressure fields, while the training for the POD filter and the autoencoder is carried out on a separate dataset of 2400 frames. The denoising autoencoder for 3D channel flow employs 11-layer 3D convolution neural networks, with max pooling to compress and transpose convolution to recover the information. The detailed architecture is illustrated in Fig. 3. The AMIC uses the weight coefficient λ at $(0.15, 0.15)$, and the total number of iterations is set to 12.

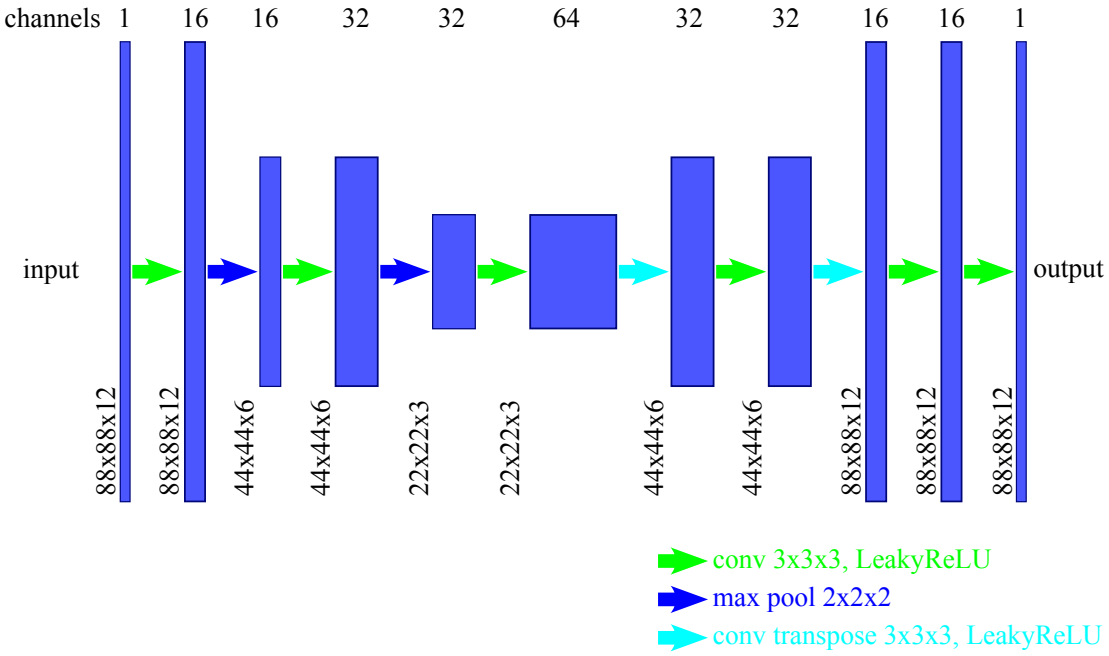

Figure 3. The architecture of the denoising autoencoder applied for the 3D channel flow simulation.

3.2. Planar PIV experiment on the wake of a wing foil

The proposed method is then evaluated using the experimental data obtained from PIV measurements in the wake of a 2D wing model with a NACA 0018 airfoil. As describes in Chen et al. (2022), the experiments are conducted in the water tunnel of Universidad Carlos III de Madrid, featuring a test section of dimensions $2.5 \times 0.5 \times 0.55m^3$. The wing has a chord length of $80mm$ and is angled at 10° to generate a moderate-intensity shedding wake, as presented in Fig. 4 (**a**) The free stream velocity is controlled to $0.06m/s$, resulting a Reynolds number at 4800.

A dual cavity pulsed Nd:YAG Quantel Evergreen laser is utilized to generate a sheet approximately $1mm$ thick. An Andor sCMOS camera with a $2560 \times 2160px^2$ sensor and a $50mm$ focal length objective is employed, set to a resolution of $8.3px/mm$. Particle images are sampled at $30Hz$, ensuring time-resolved measurements. A sliding correlation method with a 3-frame kernel is applied, resulting in a final interrogation window size of $40px$ with 75% overlap, providing a vector spacing of $1.20mm$. A 110×70 subdomain is applied in processing.

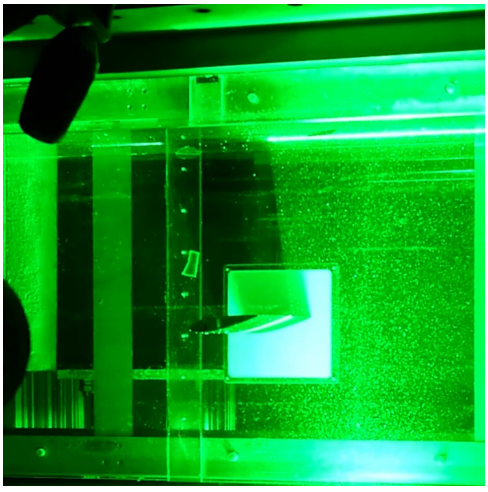

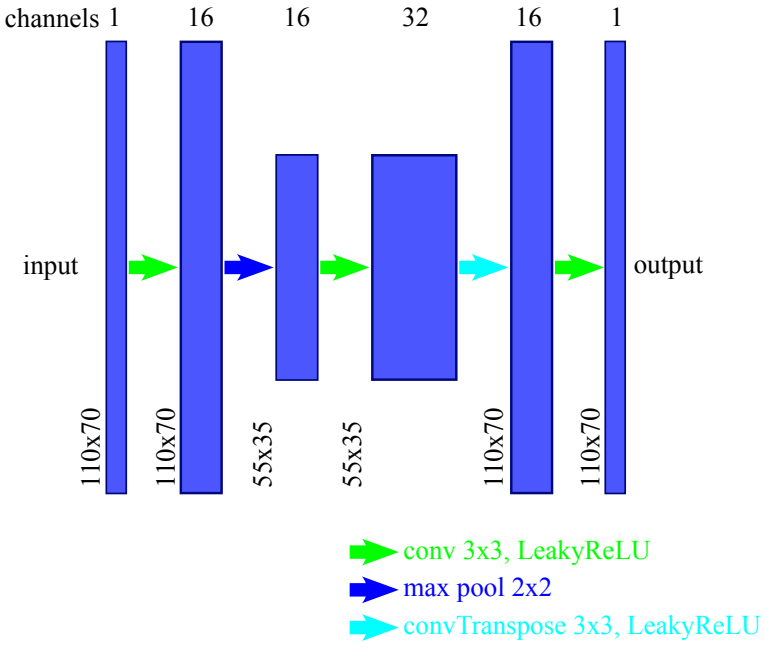

(a) (b)

Figure 4. (**a**) A photo of the experimental setup for the wake of a wing. (**b**) The architecture of the denoising autoencoder applied for the planar PIV datasets.

The denoising autoencoder for planar PIV fields in the wake of wings utilizes 6-layer convolutional neural networks. It incorporates max pooling for data compression and transposed convolution for information recovery. The detailed architecture is depicted in Fig. 4 (**b**). The AMIC algorithm employs weight coefficients λ set at $(0.1, 0.05)$, with a total iteration count of 6.

4. Result

Fig. 5 presents an instantaneous wall-normal component of velocity field from the 3D channel dataset processed using SG filter, POD truncation, denoising autoencoder and AMIC correction from the noisy field shown in Fig. 2. In terms of recovering the true velocity field from the noisy measurements, the SG filter shows good performance since it recovered most of the flow structures without distortion. The POD truncation, instead, performs remarkably worse: depending on how the truncation cut-off is set it either miss the fine-scale details of the true field or introduces instead noise contamination. This behavior can be ascribed to a lack of statistical convergence of the POD due to not enough statistical separation between field features and noise be present in the dataset: the lower-order modes which are retained by the filter are uniformly corrupted by noise while the discarded high-order modes still contain useful information. The denoising autoencoder performs well with GWN, while on the field with CGWN, the neural networks can not separate adequately flow features and noise, thus some spurious fluctuation from noise is also recovered. AMIC per-

forms quite well for both noise types, though with slightly more residual noise when compared to the result of SG filter for the GWN.

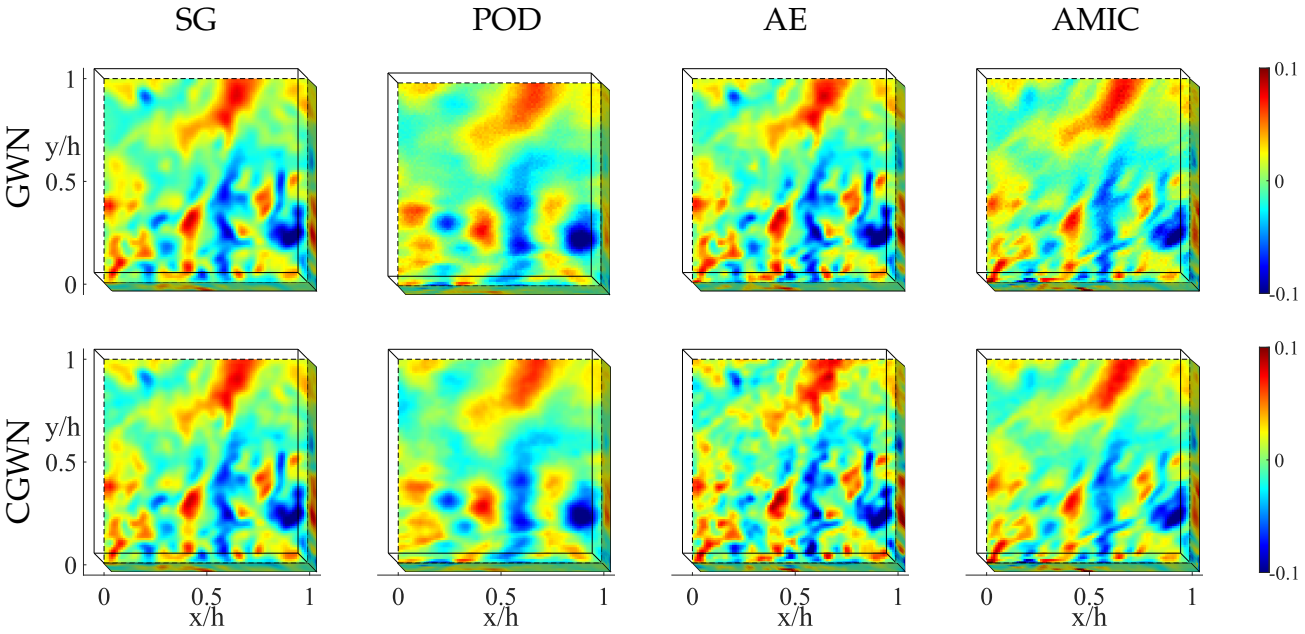

Figure 5. The wall normal component of the velocity field, after denoising. The upper row and lower represents the result of GWN and CGWN separately.

The original streamwise component of the velocity field as well as that with GWN and that after processing and the error are presented in Fig. 6. SG filter works slightly better than AMIC correction away from the wall ($y/h > 0.2$), whereas AMIC shows superior performance in the near-wall region. This can be ascribed to two factors. Firstly, SG filtering is affected by edge effects in the near-wall region. Secondly, small-scale motion is dominant in the near-wall region. When the scale is comparable to or smaller than the kernel of SG filter, the fluctuations undergo significant modulation. One the other hand, AMIC smooths the flow considering small-scale motions as frozen, thus reducing smoothing of physically-consistent features. Among the tested filters, the POD truncation exhibits the worst performances, most likely due to the challenge imposed by the small dataset size. The result of the autoencoder is similar to SG filter, with superior performance far from the wall than in the near wall region.

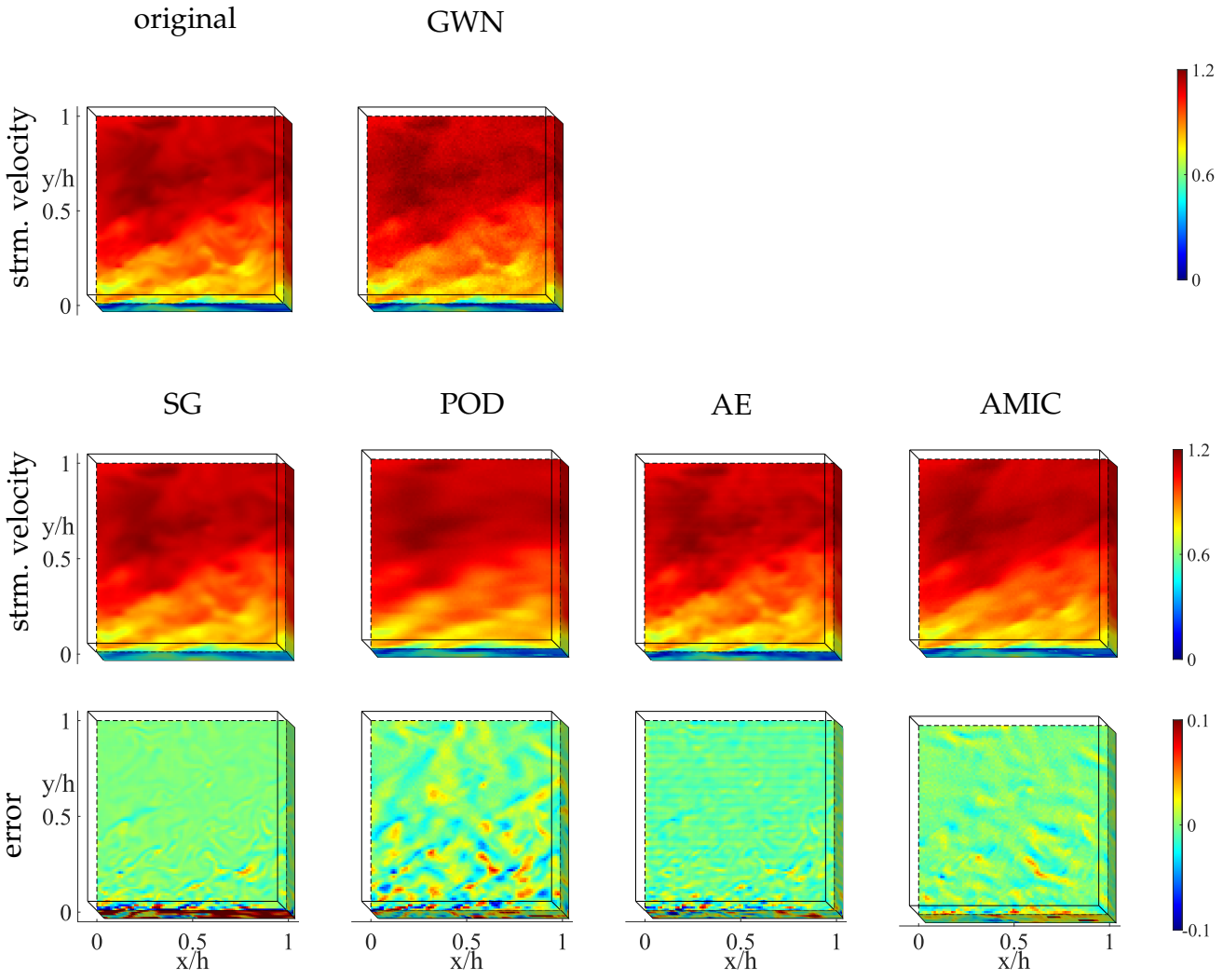

Figure 6. Top row: Streamwise component of velocity field of channel flow from the original DNS data and data superimposed with GWN. Central row: the streamwise component of the velocity field of channel flow after denoising (from left to right) with SG, POD, autoencoder and AMIC. Bottom row: error fields.

The pressure field is obtained from integration of the pressure gradient obtained plugging the time-resolved velocity data in the Navier-Stokes equation. The integration is carried out with a 3D version of the route-free iterative method described in (Chen et al., 2022), with GPU acceleration. Given the minimal fluctuations comparing to the bulk velocity in this channel flow, the pressure field is highly sensitive to uncertainties in the velocity field. Figure 7 shows the pressure fields derived from the velocity fields of the original simulation dataset and their noisy counterparts. The subsequent rows present the pressure integrated from velocity fields processed using the SG filter, POD truncation, denoising autoencoder, and AMIC under both noise types.

The POD filter fails to provide accurate pressure estimates because it does not adequately preserve small-scale motions after truncation. The pressure field estimation is also unsuccessful for the denoising autoencoder. This is likely to be addressed to errors due to filtering of small scales and no

relation in adjacent frames, which amplifies in the integration process. The SG filter performs well in estimating pressure under GWN. AMIC, however, has slightly superior performances. Under CGWN, also SG is severely challenged, while AMIC correction yields acceptable results in terms of the shape and intensity of high- and low-pressure regions. This is because CGWN, after convolution, affects scales comparable or larger than the filtering kernel of SG, thus making it difficult for the SG filter to remove them effectively. In contrast, AMIC correction accurately detects and removes noise by tracking the flow's evolution over multiple frames, maintaining only features that are consistent with the dominant physical mechanisms.

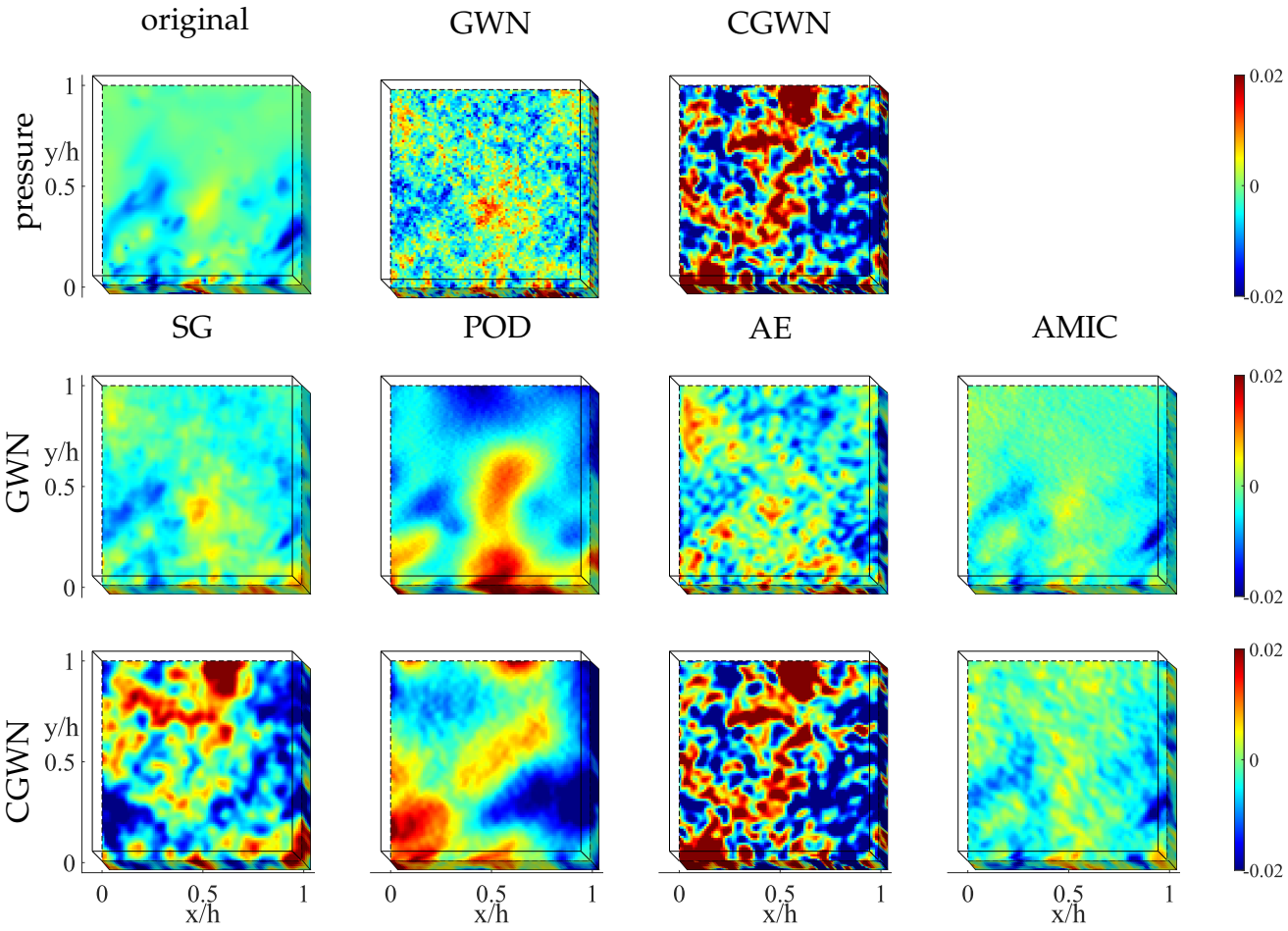

Figure 7. Top row: the pressure field of the channel flow integrated original DNS velocity field, velocity field with GWN and CGWN (from left to right). Central and bottom row: the pressure field of channel flow integrated from processed velocity fields for GWN and CGWN. From left to right, results from SG filter, POD truncation, denoise autoencoder and AMIC.

The overall RMS error of velocity and pressure fields from noisy and processed field over 100 frames are reported in Fig. 8 (**a**)&(**b**), where the error of velocity is normalized by V_b, while that for pressure is by $\frac{1}{2}V_b^2$. Furthermore, as shown in Fig. 8 (**c**)&(**d**), the results are compared in terms of

cosine similarity, defined by

$$S_{cos} = \left| \frac{\langle X, X_{ref} \rangle}{\|X\|_2 \|X_{ref}\|_2} \right|_t \tag{4}$$

where X_{ref} is the noisy-free velocity or pressure and X is the field to be counted similarity with the noisy-free field, both of them are reshaped into vectors. The S_{cos} always ranges in $[-1, 1]$, with the value closer to 1 means better similarity. The analysis confirms that SG filter, autoencoder and AMIC have similar performance in improving the velocity fieldHowever, when it comes to the accuracy of pressure field computed from velocity field, POD truncation and autoencoder fail on both GWN and CGWN, SG filter is effective only on GWN while AMIC seems robust also in presence of spatially-coherent noise.

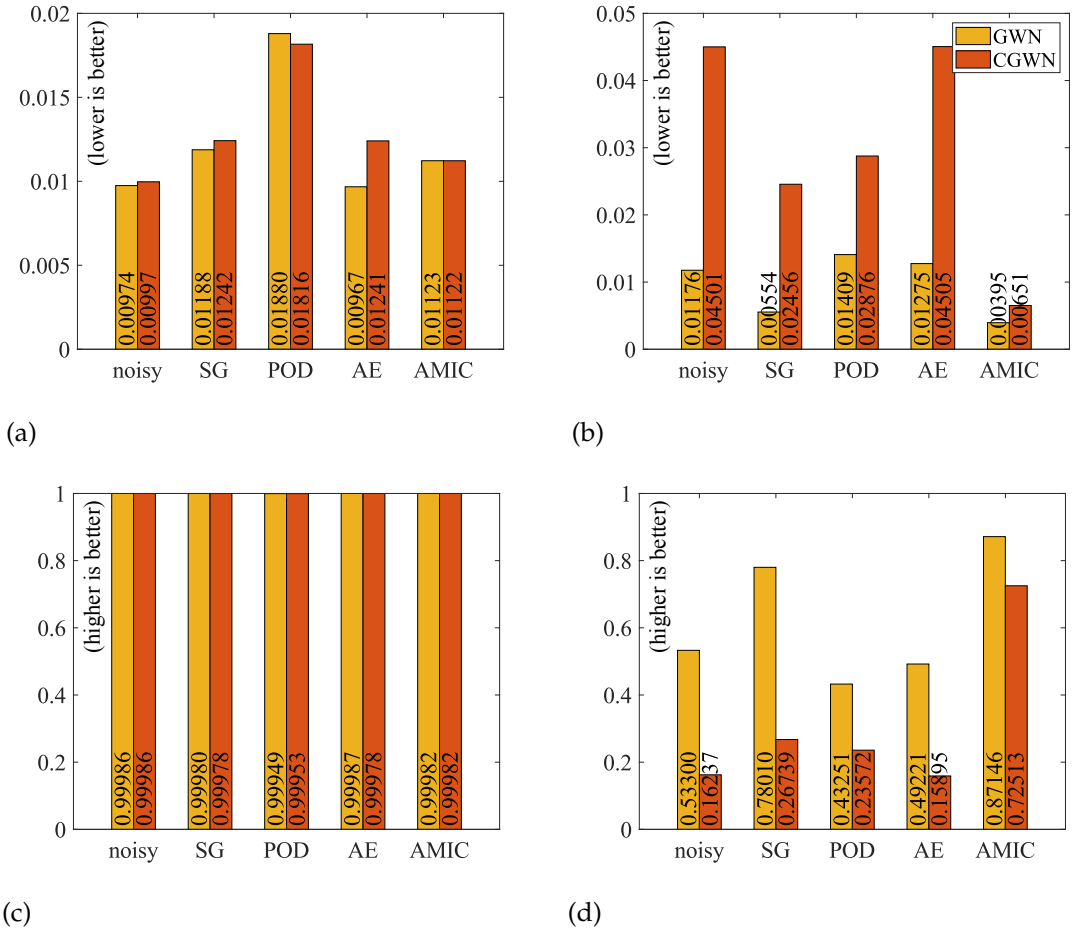

Figure 8. (**a**) RMS error from noisy and processed velocity field, (**b**) RMS error pressure computed from noisy and processed velocity field, (**c**) cosine similarity of velocity field between noisy/processed and the original one, (**d**) cosine similarity of pressure computed from velocity field between noisy/processed and the original one.

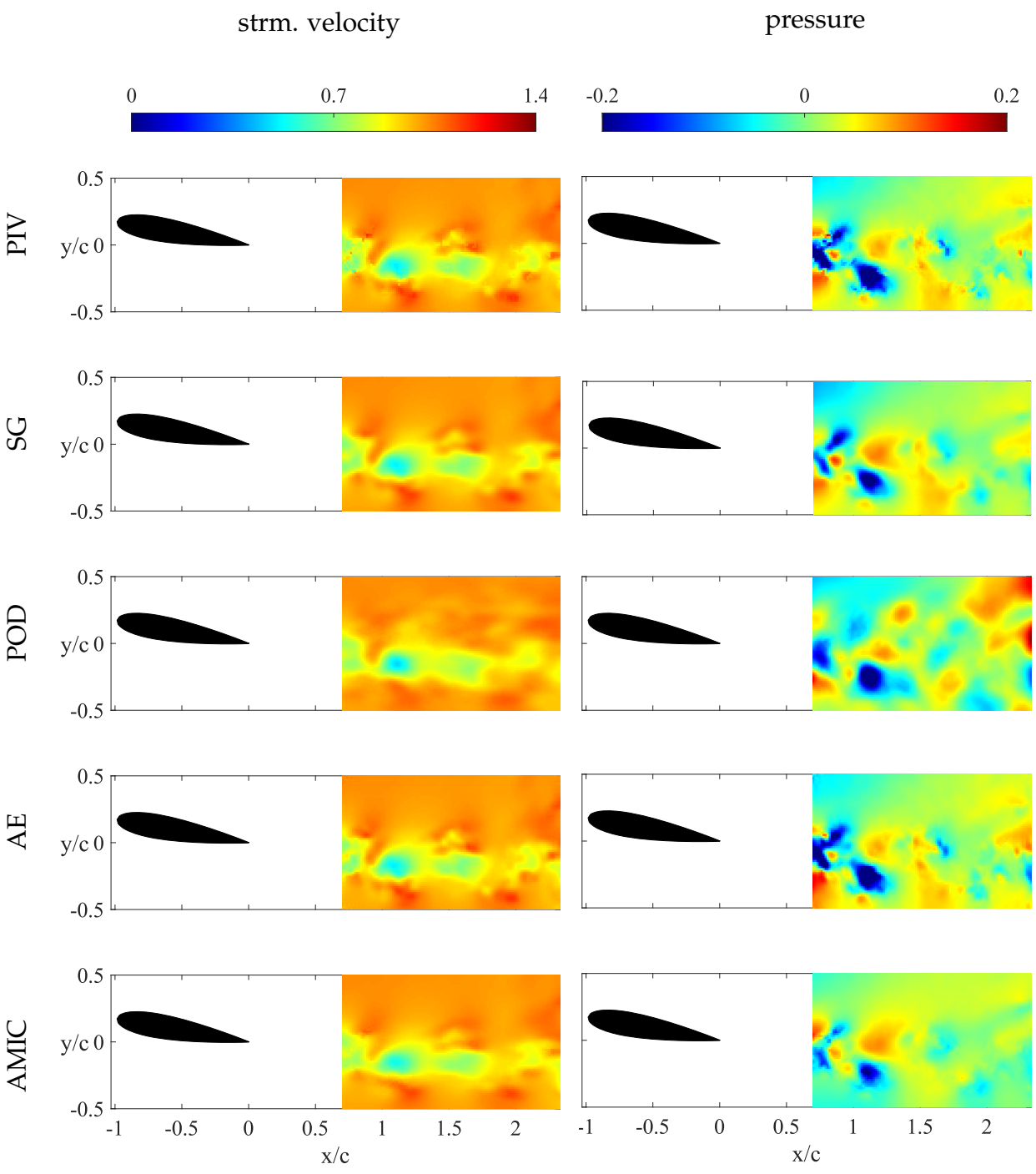

Figure 9. The streamwise component of velocity field (left) and pressure field integrated from relative velocity field (right), from the 2D wing wake dataset. From top to bottom are the result of: original PIV field, SG filtered field, POD truncated field, autoencoder denoised field and AMIC field. The velocity and pressure are normalized with the free stream velocity and dynamic pressure, respectively.

Fig. 9 presents the velocity field from the PIV experimental dataset of the wing wake, along with the results processed using the four aforementioned methods in the left column. The subsequent

pressure fields integrated from these velocity fields are also shown in the right column of the figure. The results from PIV and processed fields appear similar in this frame. The denoising autoencoder seems to preserve most of the information from the velocity field. The SG filter and AMIC exhibit slight information loss, while POD truncation shows more loss than AMIC. However, since the exact pressure field is not available in the real experiment, the pressure fields can not be evaluated using direct methods. Therefore, we proposed two indirect methods, which will be discussed in Sec. 4.1

4.1. The evaluation without true value of pressure field

The uncertainty is inevitably existing in the PIV fields, which affects the result of pressure estimation using Navier-Stokes equation, thus the true value of pressure field from PIV is technically unknown. Consequently, neither the RMS error nor the cosine similarity can be deployed to evaluate the pressure fields after processing. In this section, we proposed two indirect methods for the evaluation.

4.1.1. The residual from the temporal derivative of N-S equation

Since Navier-Stokes equation (for incompressible flows)

$$\frac{\partial \mathbf{u}}{\partial t} + (\mathbf{u} \cdot \nabla)\mathbf{u} = \nu \nabla^2 \mathbf{u} - \frac{1}{\rho}\nabla p \tag{5}$$

is used to compute the pressure, the inconsistency should be minimal, in fact, the stopping criterion for the iterative pressure calculator is either reaching 1×10^5 iterations or achieving an average residual below 1×10^{-8}. The solver only applies a 3-point central differentiation to compute the temporal derivative of velocity field, and the residual from the temporal derivative of Navier-Stokes equation,

$$Res = \left\| \rho \left(\frac{\partial^2 \mathbf{u}}{\partial t^2} + (\frac{\partial \mathbf{u}}{\partial t} \cdot \nabla)\mathbf{u} + (\mathbf{u} \cdot \nabla)\frac{\partial \mathbf{u}}{\partial t} - \nu \nabla^2 \frac{\partial \mathbf{u}}{\partial t} \right) + \nabla \frac{\partial p}{\partial t} \right\| \tag{6}$$

is not guaranteed to be little after calculating the pressure field. Thus it can serve as an index to analyse the quality of velocity and pressure field. Moreover, every item of this equation contains the temporal derivative, making it very sensitive to the variation or error along time.

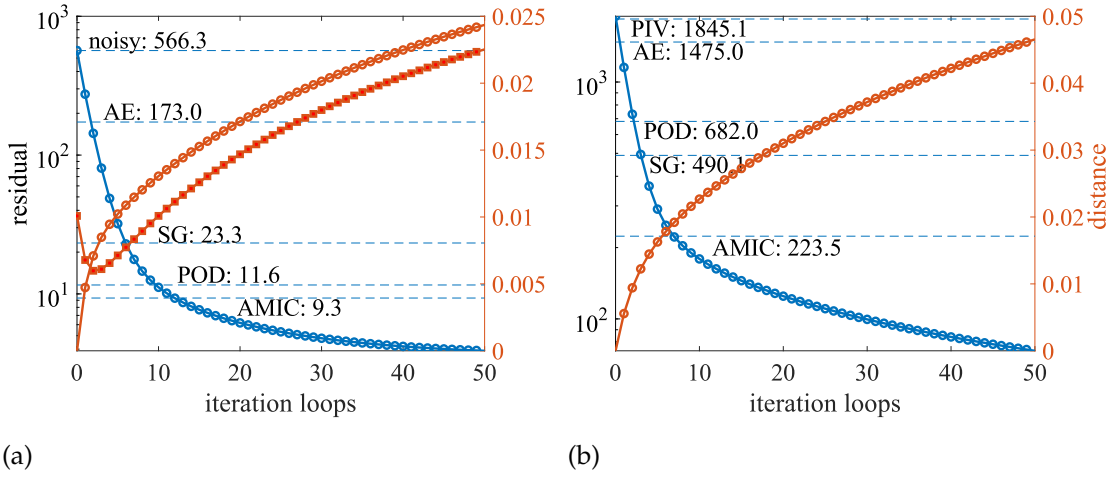

Figure 10. The figure displays the residuals from the temporal derivative of the Navier-Stokes equation (the descending blue line) and the distance to the velocity field (the ascending red line) at each iteration loop of AMIC for (**a**) the 3D channel flow, and (**b**) the planar PIV of the wing wake. The distance include those relative to the noisy or PIV field as the starting point of AMIC (indicated by red the curves with hollow red circles) and those relative to the velocity field without noise (indicated by the red curve with solid red squares). The horizontal blue line represents the residual from the noisy and processed fields.

Fig. 10 illustrates the residual from the temporal derivative of Navier-Stokes equation of AMIC from 0 to 50 iterations by the descending blue lines, for both the 3D channel simulation (with GWN) and the planar PIV datasets of the wing wake. The distances between the velocity fields in AMIC iteration and the references, normalized by the bulk or free stream velocity, are shown as ascending red lines. Specifically, the lines marked with hollow circles are using the noisy or original PIV velocity field as reference, while that marked by solid squares are referenced with noise free velocity field.

The residual decreases rapidly during the initial iteration loops and then decreases in lower speed. Initially, the distance from the noisy or original PIV velocity field is zero, as they serve as the starting point for AMIC. In the following, the distances increase with a steeper slope in the early loops, followed by rises at slower paces. On the other hand, the distance with reference to the field without noise for the channel dataset decreases in first 2 iterations, than turns to increase. This suggests that AMIC enhances both the velocity and pressure fields while introducing errors, both from the simplification of the governing equation and the error in other frames. During the initial iterations, AMIC effectively eliminates noise or errors in the velocity field, causing fast departures from the initial state and significant improvement in the pressure field. The velocity field's improvement reaches peak very soon then the contribution becomes slightly, while errors are introduced at a nearly constant rate, therefore the distance to the velocity field turns to increase after several iterations. However, the advection model continues to adjust temporal and spatial information, leading to sustained improvements in estimating the pressure field.

This trend indicates that it's preferable to halt AMIC before reaching the saturation stage of iterations. The early halting ensures significant improvement in the velocity and pressure field with minimal introduction of distortion or smoothing to the velocity field. It's recommended to determine the halting loop at the turning point or the point with maximum curvity of the residual curve, which means to set it for the channel dataset around 10 and for wing dataset around 8.

Meanwhile, the residual in Eq. (6) is calculated from noisy/PIV fields and fields processed with SG filter, POD truncation, denoising autoencoder and AMIC, where the relaxation coefficients and total iteration follows the setting in Sec. 3, and plotted using horizontal dash lines in Fig. 10. AMIC exhibits the lowest level of residual among all methods, the SG filter shows significant enhancement compared to the noisy or PIV field, although it still falls behind AMIC. The autoencoder demonstrates minimal improvement. However, the residual from POD in the channel dataset appears deceptively low, contradicting previous results. This discrepancy may be attributed to POD truncation removes too much details, making a wrong pressure prediction but compliant to the evolution of Navier-Stokes equation.

4.1.2. Flickering index

The Structural Similarity (SSIM) index is a widely-used metric for assessing image quality by comparing the structural information of two images in computer graphics. SSIM evaluates luminance, contrast, and structure, providing a single quality score that correlates well with human visual perception. However, SSIM's single-scale approach can miss important details at different resolutions. To address this, the Multiscale Structural Similarity (MS-SSIM) index was developed. MS-SSIM extends SSIM by calculating the similarity across multiple scales, capturing both local and global structural information (Wang et al., 2003). This multiscale approach offers a more comprehensive and accurate assessment of image quality, especially in applications like image compression and enhancement. The range of the MS-SSIM index is between 0 and 1. A value of 1 indicates perfect similarity, meaning they are identical in terms of perceived quality. A value closer to 0 indicates poor similarity, suggesting significant differences in structural information between the images.

The MS-SSIM is applied to evaluate the pressure field by calculating the value between two adjacent frames and then averaging, where the value is computed using the MATLAB function *multissim* for 2D and *multissim3* for 3D pressure fields, the dynamic range is set at 0.04 for the channel case and 0.4 for the wing case, as the range of colour bar for pressure fields in Fig. 7 and Fig. 9.

The value of MS-SSIM averaged over time is presented in Fig. 11. Among all methods the AMIC has the best similarity of pressure field in two adjacent frames thus indicating the flickering is suppressed. Still, like the residual from the temporal derivative of N-S equation, the value is deceptively high for POD truncation on the field superimposed with GWN. Thus it requires human discernment on the velocity and pressure fields after processing after evaluating with MS-SSIM.

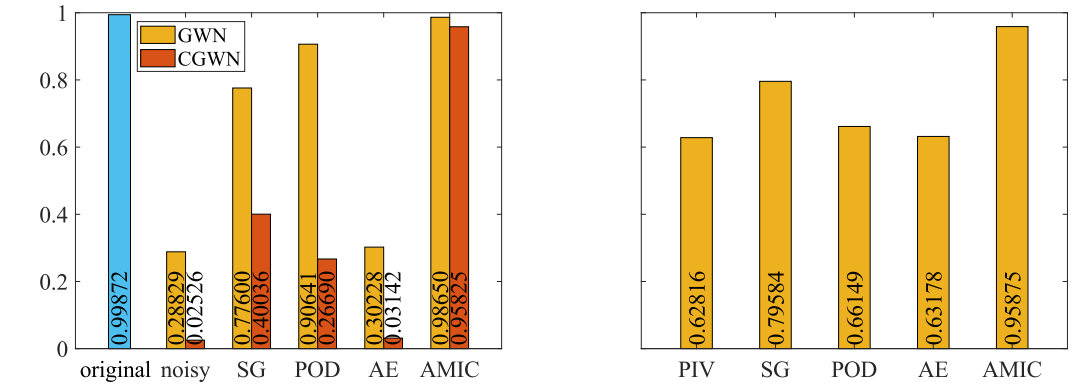

(a) (b)

Figure 11. The MS-SSIM of original, noisy, PIV and processed fields, where (**a**) shows the value from channel dataset, and (**b**) shows the value from wing dataset.

In the numerical solution of the Navier-Stokes equations for pressure, even minor fluctuations in the velocity field at a specific location can exert a non-local impact on the pressure distribution. Consequently, the integration of pressure field senses the noise added to the velocity field in the whole domain. This sensitivity often leads to nonphysical flickering in pressure, particularly noticeable at corners. Nevertheless, considering the pressure fields temporally differentiable, generally speaking, when there is no appearing/disappearing/moving shock waves, expansion fans or moving objects in the domain, the pressure field can be expanded using a Taylor series,

$$p(\mathbf{x}, t+\Delta t) = p(\mathbf{x}, t) + \frac{\partial p(\mathbf{x}, t)}{\partial t}\Delta t + \frac{1}{2}\frac{\partial^2 p(\mathbf{x}, t)}{\partial t^2}\Delta t^2 + \frac{1}{6}\frac{\partial^3 p(\mathbf{x}, t)}{\partial t^3}\Delta t^3 + o(\Delta t^3) \tag{7}$$

where the pressure field is defined as a function of both spatial coordinate $\mathbf{x}$ and time t. When the time increment is sufficiently small, the higher powers of Δt become negligible. Consequently, in a small temporal neighborhood, the Eq. (7) simplifies to,

$$p(\mathbf{x}, t+\Delta t) - p(\mathbf{x}, t) = \frac{\partial p(\mathbf{x}, t)}{\partial t}\Delta t \tag{8}$$

After discretizing Eq. (8) in space and applying the root-mean-square manipulation, the equation becomes,

$$\|p(\mathbf{x}, t+\Delta t) - p(\mathbf{x}, t)\|_2 = \left\|\frac{\partial p(\mathbf{x}, t)}{\partial t}\right\|_2 \Delta t \tag{9}$$

This implies that the 2-norm distance between pressure fields in two close snapshots, regarding each of them as a state, is proportional to the temporal interval Δt. Unlike MS-SSIM considers the 0^{th} order truncation of Eq. (7), this method can also include the 1^{st} order items.

The curves representing the distance between successive frames and the initial frame for the channel dataset are plotted in Fig. 12, with each subplot containing 192 five-frame curves, and 3 of them

are highlighted. The figure demonstrates that the pressure field from the original data maintains a proportional relationship as described by Eq. (9). In contrast, for fields with GWN, the curves of distance boom from the 0^{th} to the 1^{st} frame, then fluctuates around the level of the 1^{st} frame, indicating a sudden change in the pressure field from the 0^{th} to the 1^{st} frame, then followed by random fluctuations. The distances for the pressure field with CGWN grows more rapidly from the 0^{th} to the 1^{st} frame that run out of the box, and the following part of curves cannot be observed in the scope of figures, which can be explained as more severe changes of the pressure field frame by frame. After processing on the fields with GWN, the SG filter and POD truncation show improvement as the curves become more linear, though significant fluctuations remain. As shown in the highlighted curves, some curves of the POD result show the distance from the 0^{th} to the 2^{nd} frame being greater than from the 0^{th} to the 1^{st} or 3^{rd} frame, suggesting after the state changes from the 2^{nd} to the 3^{rd} frame, the pressure field changes in a controversial way as the distance decreases. In our observation along several successive frames, this happens when the pressure field is flickering, i.e. the pressure in the corner regions increases and decreases randomly. The autoencoder has rare improvement. The AMIC produces almost linear curves, although the dispersion is slightly larger than that of the original field. For the velocity field superimposed with CGWN, the curves of SG-filtered, POD-truncated, and autoencoder-denoised fields resemble those of the unprocessed CGWN field, exceeding the y-axis limit since the 1^{st} frame, indicating random evolution of the pressure fields. AMIC continues to produce nearly linear curves, though with a slightly larger slope and dispersion than the original field.

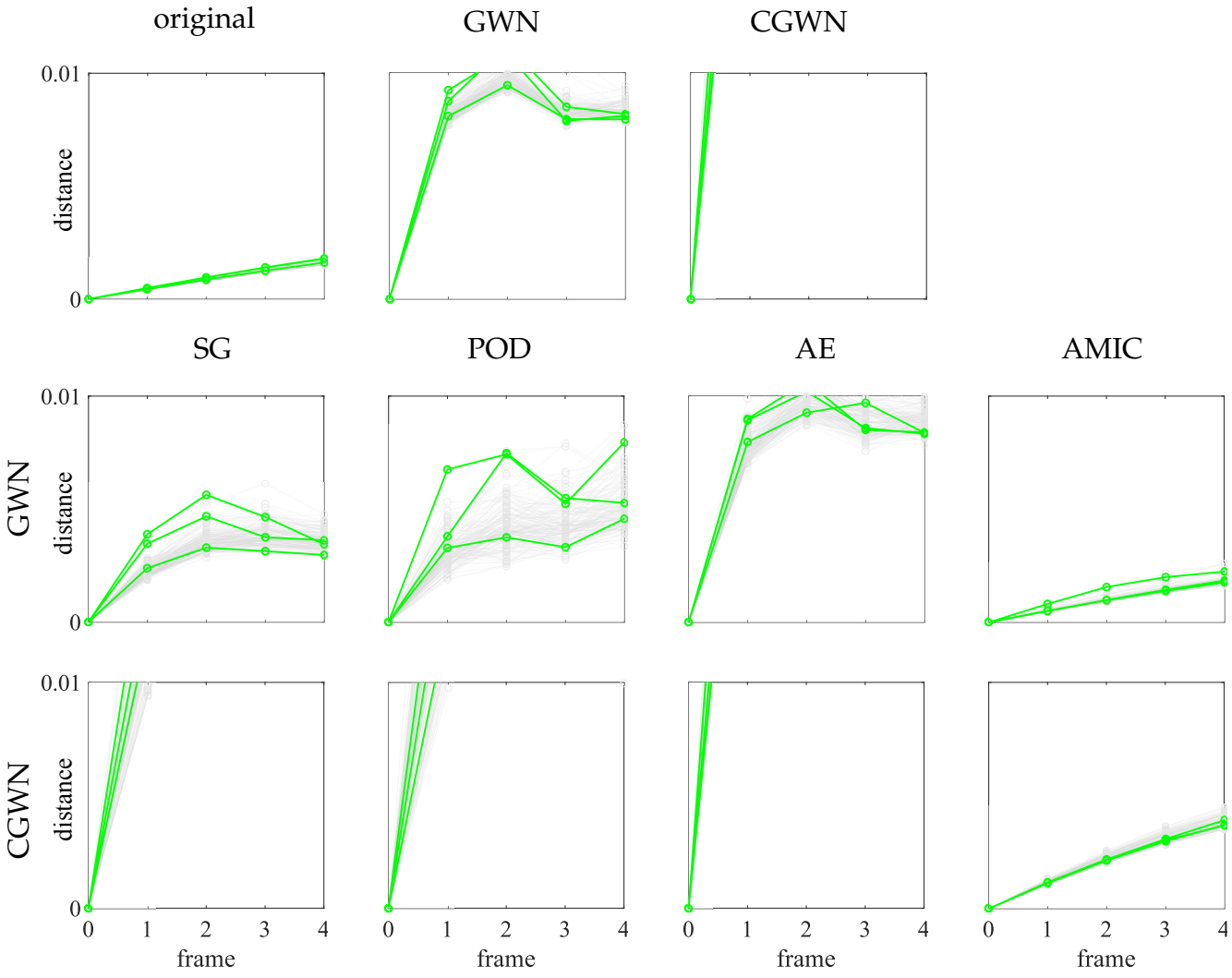

Figure 12. The distance of the pressure field as a state compared to the distance in the frame for the channel data set. The first row displays the curves of the original velocity field, the field with GWN, and the field with CGWN, from left to right. The second and third rows show the results of fields processed from GWN and CGWN imposed fields, respectively. Both rows present the outcomes of the SG filter, POD truncation, denoising autoencoder, and AMIC, from left to right. The green curves are 3 randomly chosen one among all.

The curves about the distance between the state of pressure field at the 0^{th} frame to successive frames from the PIV dataset of wing wake are illustrated in in Fig. 13. 472 five-frame sequences are plotted and 3 of them are highlighted. The random fluctuation and dispersion observed from the original PIV field are not improved using POD truncation or the autoencoder. The SG filter slightly reduces the fluctuations. Finally, AMIC provides significant improvement, resulting in the curves appearing nearly straight.

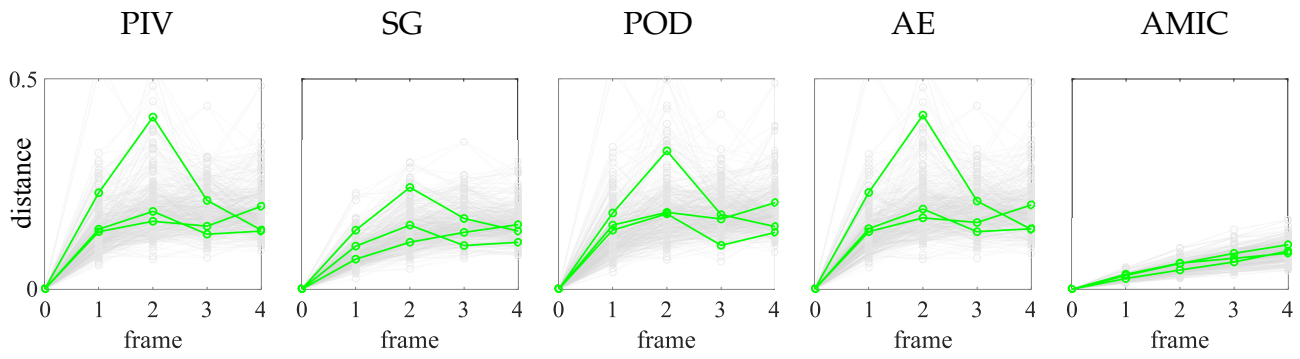

Figure 13. The distance of the pressure field as a state compared to the distance in the frame for the wing dataset. From left to right, the line chart displays the curves from the PIV, SG-filtered, POD-truncated, autoencoder denoised, and AMIC-processed fields. The green curves are 3 randomly chosen one among all.

The true value of pressure fields from real PIV measurements are unknown since they are computed from the velocity field using Navier-Stokes equation, but there is uncertainty in the PIV field. However, the linearity of the distance discussed above reveal another indirect way to evaluate the quality of pressure fields. The linearity can be quantified using the goodness of linear regression. As this distance exhibits a proportional relationship with the temporal interval, it can be expressed as $d = \alpha t$, where d represents the distance, α denotes the slope, and t signifies the temporal interval. Employing the least squares method facilitates the calculation of the slope.

$$\alpha = \frac{\mathbf{T}^T\mathbf{D}}{\mathbf{T}^T\mathbf{T}} \tag{10}$$

where $\mathbf{T}$ is a column vector containing temporal ticks, and $\mathbf{D}$ is a column vector containing distance. Then goodness of fitting (Steel et al., 1960) is given by

$$R^2 = 1 - \frac{\Sigma(d - \hat{d})^2}{\Sigma(d - \overline{d})^2} \tag{11}$$

In this context, $\hat{d}$ represents the predicted distance obtained from linear regression, while $\overline{d}$ denotes the average distance. The goodness metric, ranging from 0 to 1, reflects the quality of fit, with values closer to 1 indicating a stronger fit so that more in accordance with Eq. (9). It is important to note that linearity is a local behavior, and the slope in in Eq. (9) does not have to be a constant across all sequences. Therefore, R^2 is first calculated for each sequence and then averaged. The mean value, $\overline{R^2}$, still ranges in $[0, 1]$, with the value closer to 1 indicating that the velocity fields better fit Eq. (9). Fig. 14 shows the $\overline{R^2}$ from channel and wing wake dataset. The value from the original simulation is very close to 1, this indicates the true value for this dataset confirms Eq. 9 well within a period up to 5 frames. The $\overline{R^2}$ from the noisy and autoencoder denoised fields are close to zero, which means the pressure field experiences strong nonphysical flickering. The value is around 0.5 for SG filter under both types of noise and for POD truncation under GWN.

However, previous investigations confirms SG filter has a reasonable result but POD truncation has not. Since the $\overline{R^2}$ focuses more on nonphysical flickering in the pressure fields, some methods may offer acceptable estimation but still exhibit significant flickering, consequently their index of $\overline{R^2}$ deteriorates. This suggests that $\overline{R^2}$ can serve as a reference, but in real experiments, the velocity and pressure field should still be observed directly. AMIC achieves a $\overline{R^2}$ of around 0.99, very close to the original field's value of 0.999, indicating that AMIC significantly cancels the flickering. The pressure measurement from the real PIV experiment on the wing's wake have been already depicted in Fig. 9, however it's impossible to confirm whether the methods have good pressure estimation or not from a single frame since all of them look reasonable. On the other hand, concerning about the flickering index $\overline{R^2}$, AMIC increases $\overline{R^2}$ from 0.39 to 0.97, while the best conventional method can only increase it to 0.63, showing AMIC has significant improvement comparing to other methods tested.

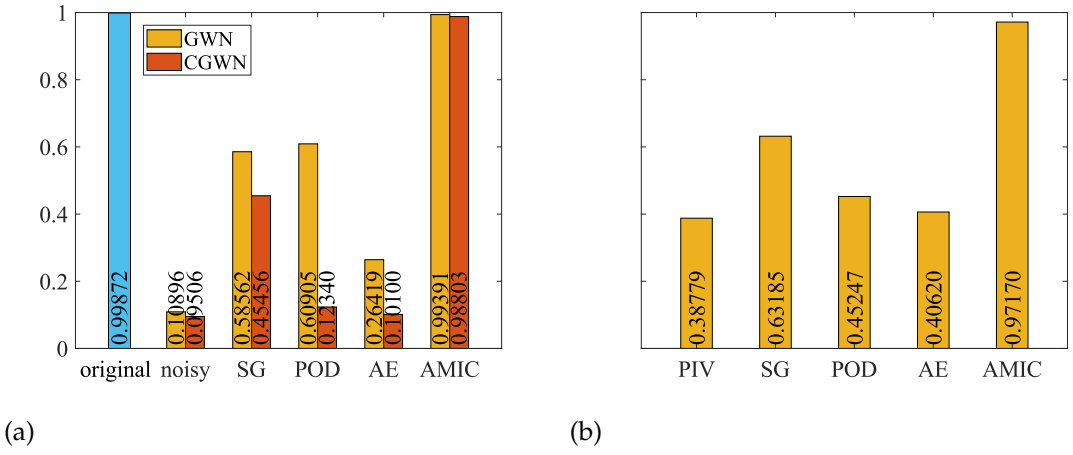

Figure 14. The $\overline{R^2}$ computed from individual curves using Eq. (11) of original, noisy, PIV and processed fields, where (**a**) shows the value from channel dataset, and (**b**) shows the value from wing dataset.

5. Conclusions

We proposed the AMIC method to correct time-resolved PIV fields with noise or uncertainty using a physical advection model, where small-scale motions are advected by large-scale motions. This iterative correction smooths over multiple parallel time-series of the original and propagated velocity fields. The method is tested on a 3D simulation of channel flow and a planar PIV measurement of the wake of a wing foil. We also introduced two indices to evaluate the quality of the pressure field without knowing the true value.

The AMIC correction offers two main benefits. First, it does not use a traditional filter to smooth the field that, but make the filter work on an additional dimension along the time-series of velocity fields propagated, thus preserves most flow details compared to conventional filters. Second,

AMIC leverages temporal information to refine spatial distribution and uses spatial information to enhance temporal evolution. This dual correction strategy minimizes errors in both temporal and spatial derivatives within the Navier-Stokes equation, resulting in excellent pressure estimation from noisy velocity fields. In our tests, AMIC provided significant improvements in correcting the velocity and pressure fields, particularly when the artificial noise had spatial coherence. Additionally, AMIC significantly reduced nonphysical flickering in the pressure field calculated using the Navier-Stokes equation.

Moreover, the proposed AMIC method can be easily modified to use other governing equations to propagate the velocity field. The simplistic advection-based model can be replaced by more refined advection models, VIC, or the Navier-Stokes equations. This flexibility allows the method to be tailored to specific flow studies, reducing errors in velocity and pressure field estimation in particular cases.

Acknowledgements

This project has received funding from the European Research Council (ERC) under the European Union's Horizon 2020 research and innovation programme (grant agreement No 949085). Thanks for the discussion with Professor Stefano Dicsetti and Marco Raiola from Universidad Carlos III de Madrid.

References

Azijli, I., Sciacchitano, A., Ragni, D., Palha, A., & Dwight, R. P. (2016). A posteriori uncertainty quantification of piv-based pressure data. *Experiments in Fluids*, *57*, 1–15.

Chen, J., Raiola, M., & Discetti, S. (2022). Pressure from data-driven estimation of velocity fields using snapshot piv and fast probes. *Experimental Thermal and Fluid Science: International Journal of Experimental Heat Transfer, Thermodynamics, and Fluid Mechanics*, 136.

Christiansen, I. (1973). Numerical simulation of hydrodynamics by the method of point vortices. *Journal of Computational Physics*, *13*(3), 363–379.

de Kat, R., & Ganapathisubramani, B. (2012). Pressure from particle image velocimetry for convective flows: a taylor's hypothesis approach. *Measurement Science and Technology*, *24*(2), 024002.

de Silva, C. M., Philip, J., & Marusic, I. (2013). Minimization of divergence error in volumetric velocity measurements and implications for turbulence statistics. *Experiments in fluids*, *54*, 1–17.

Foucaut, J.-M., & Stanislas, M. (2002). Some considerations on the accuracy and frequency response of some derivative filters applied to particle image velocimetry vector fields. *Measurement Science and Technology*, *13*(7), 1058.

Gesemann, S. (2015). From particle tracks to velocity and acceleration fields using b-splines and penalties. *arXiv preprint arXiv:1510.09034*.

Gu, F., Discetti, S., Liu, Y., Cao, Z., & Peng, D. (2024). Denoising image-based experimental data without clean targets based on deep autoencoders. *Experimental Thermal and Fluid Science*, *156*, 111195.

He, C., Zeng, X., Wang, P., Wen, X., & Liu, Y. (2024). Four-dimensional variational data assimilation of a turbulent jet for super-temporal-resolution reconstruction. *Journal of Fluid Mechanics*, *978*, A14.

Kramer, M. A. (1991). Nonlinear principal component analysis using autoassociative neural networks. *AIChE journal*, *37*(2), 233–243.

Lemke, M., & Sesterhenn, J. (2016). Adjoint-based pressure determination from piv data in compressible flows—validation and assessment based on synthetic data. *European Journal of Mechanics-B/Fluids*, *58*, 29–38.

Li, Y., Perlman, E., Wan, M., Yang, Y., Meneveau, C., Burns, R., … Eyink, G. (2008). A public turbulence database cluster and applications to study lagrangian evolution of velocity increments in turbulence. *Journal of Turbulence*, *9*(31).

Liu, B., Tang, J., Huang, H., & Lu, X.-Y. (2020). Deep learning methods for super-resolution reconstruction of turbulent flows. *Physics of Fluids*, *32*(2).

Lumley, J., Yaglom, A., & Tatarski, V. (1967). Atmospheric turbulence and radio wave propagation. *Journal of computational Chemistry*, *23*(13), 1236–1243.

Raiola, M., Discetti, S., & Ianiro, A. (2015). On piv random error minimization with optimal pod-based low-order reconstruction. *Experiments in fluids*, *56*(4).

Savitzky, A., & Golay, M. J. (1964). Smoothing and differentiation of data by simplified least squares procedures. *Analytical chemistry*, *36*(8), 1627–1639.

Scarano, F., Schneiders, J. F., Saiz, G. G., & Sciacchitano, A. (2022). Dense velocity reconstruction with vic-based time-segment assimilation. *Experiments in Fluids*, *63*(6), 96.

Scherl, I., Strom, B., Shang, J. K., Williams, O., Polagye, B. L., & Brunton, S. L. (2020). Robust principal component analysis for modal decomposition of corrupt fluid flows. *Physical Review Fluids*, *5*(5), 054401.

Schneiders, J. F. G., Dwight, R. P., & Scarano, F. (2014). Time-supersampling of 3d-piv measurements with vortex-in-cell simulation. *Experiments in Fluids*, *55*(3), 1692.

Sciacchitano, A. (2019). Uncertainty quantification in particle image velocimetry. *Measurement Science and Technology*, *30*(9), 092001.

Sperotto, P., Pieraccini, S., & Mendez, M. A. (2022). A meshless method to compute pressure fields from image velocimetry. *Measurement Science and Technology*, *33*(9), 094005.

Steel, R. G. D., Torrie, J. H., et al. (1960). Principles and procedures of statistics. *Principles and procedures of statistics.*.

Van der Kindere, J., Laskari, A., Ganapathisubramani, B., & De Kat, R. (2019). Pressure from 2d snapshot piv. *Experiments in fluids*, *60*, 1–18.

Wang, Z., Simoncelli, E. P., & Bovik, A. C. (2003). Multiscale structural similarity for image quality assessment. In *The thrity-seventh asilomar conference on signals, systems & computers, 2003* (Vol. 2, pp. 1398–1402).

Zhang, J., Bhattacharya, S., & Vlachos, P. P. (2022). Uncertainty of piv/ptv based eulerian pressure estimation using velocity uncertainty. *Measurement Science and Technology*, *33*(6), 065303.